A compliant mechanism with variable stiffness achieved by rotary actuators and shape-memory alloy

Adel Mekaouche, Frédéric Chapelle, Xavier Balandraud

A compliant mechanism with variable stiffness achieved by rotary actuators and shape-memory alloy

Adel Mekaouche, Frédéric Chapelle, Xavier Balandraud

Abstract The aim of this article is to study the consequences of the active stiffening of a compliant mechanism on the workspace created by the deformation of its structure. In connection with recent soft robotics research integrating shape-memory alloys (SMAs), the variation in stiffness over time is here obtained by the thermal activation of a nickel–titanium SMA spring. The workspace is created by the deformation (in the strength of materials sense) controlled by two rotary actuators acting on a structure comprising two angled flexible beams. In addition to a natural variation in the elasticity modulus of the SMA component during its thermal activation, its shape reconfiguration adds a structural deformation modifying the workspace. The existence of a common area between the workspaces of the mechanism corresponding to the non-activated and activated modes of the SMA is preserved. Several compliance maps are determined from measurements using a laser tracker targeting a given position of the loaded structure. The impact of SMA pre-stretch on stiffness variability is compared to that of a change in Young's modulus. Variations in the stiffness distributions between the two modes reveal interesting properties (stiffness sign inversion, anisotropy) for the future optimal design of compliant mechanisms with high versatility, associating the spatial positions of the effector with variable stiffness values.

Keywords Compliant mechanism · Shape memory alloy · Variable stiffness · Compliance map · Experimental validation

A. Mekaouche · F. Chapelle (✉) · X. Balandraud
Université Clermont Auvergne, CNRS, SIGMA Clermont, Institut Pascal, F-63000 Clermont-Ferrand, France
e-mail: Frederic.Chapelle@sigma-clermont.fr

1 Introduction

Compliant mechanisms are comprised of mechanical structures whose flexibility is used as a support for the generation of movements [1, 2]. The study of their behavior has given rise to considerable interest in the robotics community, for analysis/modeling [3–8] or structural synthesis [9–16]. Among these studies, a recent orientation concerns their potential for reconfigurability [17], in particular from the point of view of the variation over time in the stiffness distribution. This is a different concept from the kinematic reconfigurability of articulated machines using a rearrangement of their connectivity or the mobility of their parts. Technologies for variable stiffness have been proposed in different devices:

- stiffness adjustment assemblies, mainly located at mechanism linkages, such as in variable impedance actuators [18]. These use elastic parts integrated into conventional poly-articulated devices,

- techniques intended for soft robots: stiffening, commonly used to lock a shape after the compliant structure has conformed to the environment. This stiffening can use various types of active materials [19], including shape-memory alloys (SMAs). A major advantage to choosing SMAs is the abundant literature already available on the modeling and control of their behavior [20–23]. Their development within compliant mechanisms [24–28] has resulted in the design of actuators [29–33], mobile or inspection robots [34–38] and gripping components [39–42]. Examples of applications with variable stiffness can be found in the literature for mechanism stabilization [43, 44], vibration reduction [45, 46], integration in joints [47, 48], active fibers (fabrics) or composites [49–52].

As a contribution to the applications of SMAs, we aim to make progress towards the possibility of defining compliant mechanisms' versatile operative tasks, consisting of associating the spatial positions of the effector with variable stiffness values for each position. With respect to this mid-term objective and as a first assumption, we want to show the feasibility of varying stiffness over time in a consistent *pseudo-workspace* (PWS) obtained by the segment deformation of a compliant structure. As in Ref. [53], we use the notion of pseudo-workspace of a flexible structure. It is similar to the position workspace of a poly-articulated mechanism: they both correspond to all the positions reachable by a given point of the structure subjected to actuating forces. In the following, we use the term *pseudo* to recall that the finite displacements of the given point are obtained by deformation of the flexible arms. Moreover, the notion of consistence is defined by the need to have a common area between the PWS corresponding to each different stiffness value, the amplitude of variation being the widest possible. The SMA spring integrated into its structure makes it possible to change the stiffness at the effector position by thermal activation, leading to a variation in internal stresses and strains. The activation of the variation in stiffness can therefore be accompanied by an additional deformation of the structure, which modifies this PWS and threatens its consistency. The present study addresses the consequences of SMA-driven stiffness variability on the compliant mechanism's PWS by using compliance maps.

The compliance maps enable the specific patterns of the active compliance variation in the PWS to be visualized. Compliance or stiffness maps are usually used in poly-articulated mechanisms in order to prepare the positioning of the objects to be manipulated or to optimize trajectories in the static workspace of a machine [54–57]. The second assumption we wish to check here is the fact that these patterns carry information that could not easily be included in an equation. This will have an interest in the future by using the maps as an evaluation tool in optimization processes (not addressed here). We already started moving towards this logic in a previous work for the identification of the parameters of a poly-articulated robot [58].

Following some preparatory studies showing the value of this approach from numerical analyses [53, 59], the present paper provides first experimental results. Section 2 describes the constructed mechanism, the properties of the used SMA component, its operating mode, as well as the set-up to build experimental compliance maps. Section 3 gives details of the results obtained in terms of compliance maps, their variation when activating the SMA component, and provides a comparaison with the results predicted by the model.

2 Materials and methods

2.1 Presentation of the compliant mechanism

Figure 1a, b shows the Catia model used for the design of the device and a picture of the constructed physical system, respectively. Two arms constituted a closed kinematic chain in the vertical plane (**x**, **y**). This demonstrator was designed to carry out a concept study on a particular aspect of the functioning of compliant mechanisms: the behavior of variable stiffness over time obtained by an active material within the pseudo-workspace created by the deformation of the arms. The structural architecture was chosen to maximize the observation potential of interesting phenomena with respect to stiffness along the **x** and **y** axes, under a -**y** load (the SMA component is oriented mainly along **y**). The arms were made of thin steel beams and bent into their final angled shape to increase flexibility. These beams were connected at their upper ends by a revolute joint and attached to the

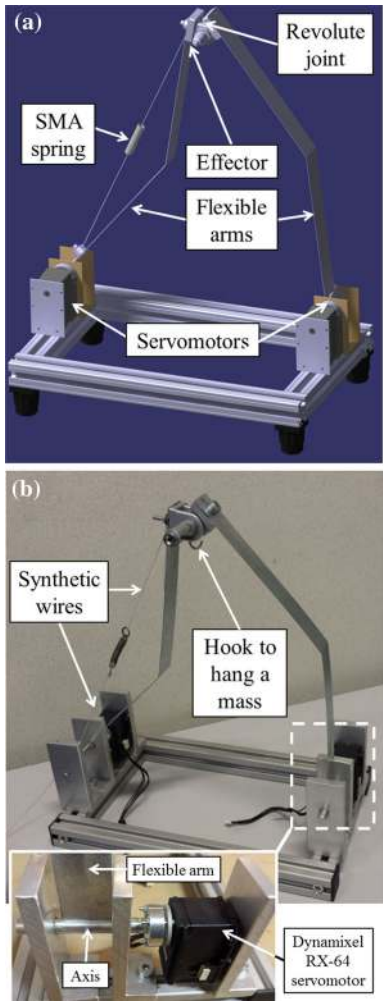

Fig. 1 Mechanical structure designed and prototyped: **a** CAD model, **b** physical demonstrator

frame with a connection to two rotary actuators (servomotors). A SMA component was attached to the extremities of one of the arms. This mechanism is based on the concept described in our previous numerical study [53]. Some adaptations were made with respect to construction constraints (see Fig. 2):

- the actuators were controlled by angular position setpoints. The scan was effected by varying the angles θ_A and θ_B of the servomotors within intervals $[\theta_{Amin}, \theta_{Amax}]$ and $[\theta_{Bmin}, \theta_{Bmax}]$,
- the passive upper revolute joint located at point C, acting as an effector, was an Arcane component made of aluminum alloy. It was assembled with the arms, unlike the numerical model where it was represented by a point. This resulted in the appearance of the geometrical parameter L_p (see Fig. 2b),
- the other differences concerned a reduction in the demonstrator size: total height $H' > H$ and total width $L' < L$,
- the motor transmission system, detailed in Fig. 1b.

The position of point C of the non-deformed configuration was chosen as the origin of the base (**x**, **y**). It can be remarked that if we model the flexibility of the beams by two revolute joints positioned at the two angled sections (angles θ in Fig. 2, varying within very short ranges), the structural deformation of this compliant mechanism is equivalent to a 5-bar planar mechanism with two degrees of freedom. Tables 1 and 2 provide the geometric and material parameters of the mechanism and the characteristics of the motors, respectively.

2.2 Presentation and characterization of the SMA component

The SMA component between points A and C (see Fig. 2) consisted of a nickel–titanium (Ni–Ti) spring provided by Nimesis Technology (France), and two synthetic fiber wires, attached one at each end of the SMA component. These wires can be considered as inextensible with respect to the deformation of the SMA spring. The mechanical properties of SMAs are due to a reversible phenomenon of solid-solid phase transformation driven by stress and temperature. The reader is referred to Refs. [20–22] for a general presentation of these materials. Briefly, the "high temperature" and "low temperature" phases are respectively called austenite (A) and martensite (M): see the phase diagram in the stress-temperature plane in Fig. 3. A given SMA is thus characterized by four transformation temperatures:

- austenite-start (As) and austenite-finish (Af), which are respectively the temperatures of the beginning and the end of the $M \rightarrow A$ transformation (corresponding to the memory effect),
- martensite-start (Ms) and martensite-finish (Mf) for the reverse transformation $A \rightarrow M$.

It should be noted that the crystallographic network in the martensite phase can have different orientations in

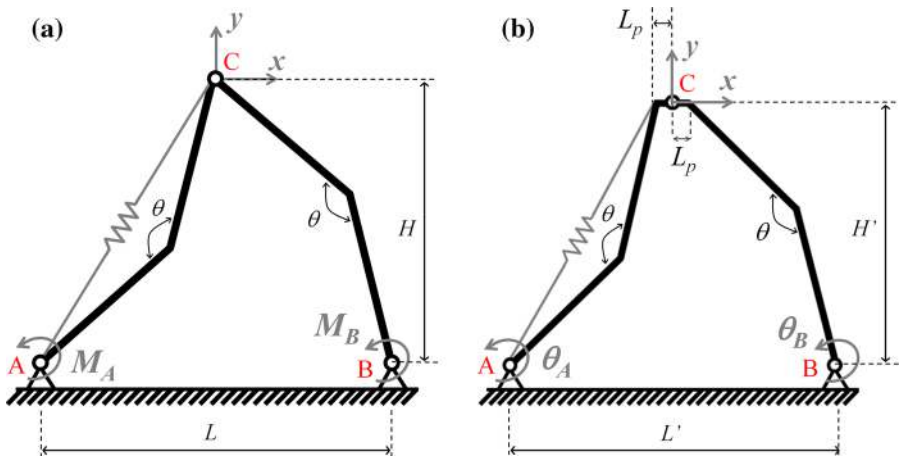

Fig. 2 Schematic view of the device: **a** corresponding to the numerical analysis in Ref. [53], **b** modified due to construction constraints

Table 1 Geometric and material parameters of the demonstrator

Parameter	Value
Total height, H'	320 mm
Total width, L'	320 mm
Arm width (in **z** direction), l	30 mm
Arm thickness, e	0.8 mm
Arm folding angle, θ	150°
Width of upper revolute joint, L_p	22.5 mm
Material of upper revolute joint	Aluminum alloy
Material of flexible arms	Steel

Table 2 Specifications of the two servomotors at A and B (see Fig. 2)

Specification	Description
Type	Dynamixel RX-64
Reduction ratio	200:1
Operating voltage	12–18.5 V
Stalling torque	5.3 N m (at 18.5 V, 2.6 A)
Starting current	2.1 A
No load speed	64 rpm (at 18.5 V)
Minimum angle	0.29° × 1024
Operating range	Actuation: [0°, 300°]
	Wheel: continuous rotation
Material	Full metal gear, plastic body
Dimensions	40.2 mm × 61.1 mm × 41 mm
Operating T°	5–80 °C

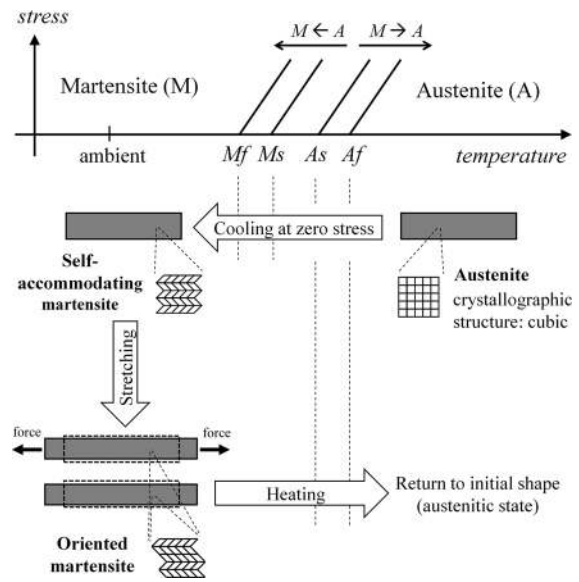

Fig. 3 Simplified SMA state diagram, and steps of the memory effect

space with respect to the austenite crystal, corresponding to several so-called martensite variants. Two cases can be distinguished:

- when the different variants are present in equal proportions in the SMA, the macroscopic deformation is close to zero with respect to the austenitic shape at zero stress (considered as the reference configuration). Such a martensite is said to be self-accommodating,
- the stretching of the SMA sample is accompanied by a change in the proportions of martensite variants, leading to a macroscopic deformation,

which is maintained when unloading the sample. Such a martensite is said to be oriented. A return to the austenite phase by heating causes a return to the initial shape of the SMA, corresponding to the so-called memory effect.

We used the SMA spring only in its linear elastic responses: either purely austenite, or a fixed martensitic state after pre-stretching (linear portion of the force-displacement curve, as in Fig. 4). By fixed martensitic state, we mean a given level of oriented martensite. Table 3 provides the dimensional, mechanical and thermal parameters of the SMA spring used for the demonstrator. Ambient temperature for the tests was about 20 ° C. The SMA was thus fully martensitic at ambient temperature as $Mf > 20\,^{\circ}$ C. The full self-accommodating martensitic state was obtained by first heating the spring above *Af* (full transformation to austenite) and returning to ambient temperature without any load applied to the spring.

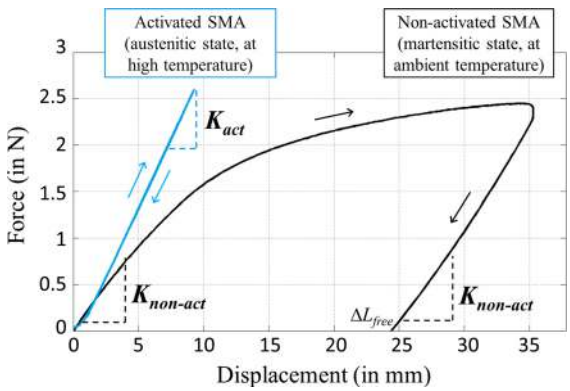

Fig. 4 Force-displacement curve of the SMA spring in martensitic state (non-activated state, i.e. at ambient temperature) and in the austenitic state (activated state, i.e. at high temperature)

To complement this information on the SMA spring, we performed stiffness characterization tests using a uniaxial tensile machine for each of the two states of the SMA (martensitic and austenitic). A direct current heating power supply was used to heat the SMA spring. The voltage and the current were equal to 24 V and 3 A, corresponding to an electrical power passing through the SMA spring of 72 W. This power was sufficient for a total transformation from martensite to austenite within a few seconds. Load-unload traction tests were force-driven with a maximum value of 2.5 N. The cycle time was set at 30 s, giving a speed V_{load} of ± 0.166 N/s. Figure 4 shows the force-displacement curves obtained:

- in the **activated state** (> 70 °C, i.e. in austenitic state), the mechanical response (force versus displacement) was elastic and linear, with a stiffness $K_{act} = 0.308$ N/mm,
- in the **non-activated state** (at ambient temperature, i.e. in martensitic state), a stiffness $K_{non-act} = 0.166$ N/mm was measured. As expected, stretching was accompanied by the appearance of oriented martensite: see residual displacement at the end of the mechanical cycle. The free length of a spring is defined by its length at zero force (i.e. without any external force). We note that this length is directly related to the proportion of martensite variants, corresponding to the shape taken by the spring when loaded and unloaded at ambient temperature. Additional tests were carried

Table 3 Dimensional, mechanical and thermal characteristics of the Ni–Ti SMA spring

Parameter	Value
Number of active coils	21
Diameter of the wire	1 mm
Free length of the springin the austenitic state (above *Af*)	44 mm[a]
Total free length L_{AC} (SMA spring + two wires)	314 mm
Martensite-finish temperature, *Mf*	> 30 °C
Martensite-start temperature, *Ms*	> 30 °C
Austenite-start temperature, *As*	55 °C
Austenite-finish temperature, *Af*	70 °C
Stiffness in the non-activated state (martensite), $K_{non-act}$	0.165 N/mm[b]
Stiffness in the activated state (austenite), K_{act}	0.308 N/mm[b]

[a]Equal to the free length at the self-accommodating martensitic state (below *Mf*)

[b]Identified from Fig. 4

out to identify the variation in stiffness as a function of the level of martensite orientation. Four mechanical cycles were performed by gradually increasing the maximum loading level. Stiffness $K_{non-act}$ was measured for each loading stage. Table 4 gives the values of $K_{non-act}$ as a function of the free length of the spring (ΔL_{free}), showing that the value of the stiffness of the SMA spring varies little with the level of martensite orientation.

As a result, a stiffness ratio $K_{act}/K_{non-act}$ of 1.85 was measured between the two states of the SMA spring (austenite and martensite).

Table 4 Stiffness values for the SMA spring in the martensitic state, with respect to the free length of the spring (corresponding to different levels of martensite orientations)

ΔL_{free} (mm)	$K_{non-act}$ (N/mm)
0 (self-accommodating state)	0.166
2.5	0.177
4.1	0.177
10.5	0.160
Average	0.165

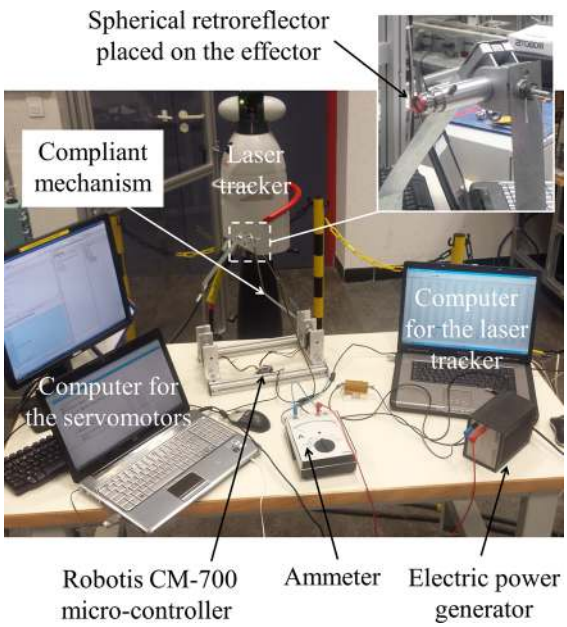

Fig. 5 Experimental set-up

2.3 Experimental protocol

Figure 5 shows the experimental system. It can be broken down into three functional subsets:

1. Control of the servomotors. A Robotis CM-700 microcontroller was used to control both actuators at A and B (see Fig. 2b). Two ranges of angle values were set for each of the actuators: $\theta_A \in [-12°, +12°]$ and $\theta_B \in [-12°, +12°]$. The origins of the angles were chosen to correspond to the no-load configuration. The scan included 11 angle values for each interval.
2. Measurement of the effector positions. The coordinate measurement tool was a Leica ATD-901 laser tracker, capturing the position of a spherical reflector mounted on a target backing.
3. Power generator and ammeter for the heating of the SMA component.

External loading for the deformation of the structure was applied in the vertical direction **y**: in practice, a mass was suspended by a hook from the axis of the upper revolute joint. The compliance maps were developed for two free lengths of the SMA spring at ambient temperature, i.e. at the martensitic state (see Table 5):

- case #1: a first test campaign was carried out with the SMA component placed in the structure in an oriented martensitic state, i.e. with a pre-stretch with respect to the reference state (austenitic or self-accommodating state). After some preliminary tests, we chose a pre-stretch of 6% because recoverable strains for Nickel-Titanium SMA straight wire are typically of 5–6%. This pre-stretch is recoverable by thermal activation of the memory effect,

Table 5 Initial state of the martensitic SMA component for the two experimental campaigns

Case	Parameter	Value
#1	Initial martensitic state	Oriented
	Pre-stretch	6%
#2	Initial martensitic state	Self-accommodating
	Pre-stretch	0%

- case #2: a second series was performed with the SMA spring in a self-accommodating martensitic state, i.e. without pre-stretch with respect to the reference state. As a consequence, there was no relative pre-displacement to be recovered upon heating (no memory effect obtained). The objective of this second series was to assess the sole influence of the change in the SMA Young's modulus between martensite and austenite.

For test campaign #1, the steps of the experimental protocol are as follows:

Implementation at ambient temperature

1. An electrical current is passed through the SMA spring while it is disassembled from the structure to reset it to the memorized length, i.e. in the austenitic state (44 mm, see Table 3).
2. The SMA spring returns to ambient temperature and passes to the martensitic state while maintaining its length (self-accommodating martensite).
3. The structure is placed in its reference position by resetting the servomotors to the origin angular values. The location of point C corresponds to the origin of the frame ($x = 0$, $y = 0$).
4. The SMA component is pre-stretched by 6%. The pre-stretch ΔL_{free} of the SMA spring is then equal to $L_{AC} \times 6/100 = 18.8$ mm. The new free length of the spring is thus 44 + 18.84 = 62.84 mm. This step is omitted for test campaign #2.
5. The SMA component is placed on the structure: see Fig. 6a.

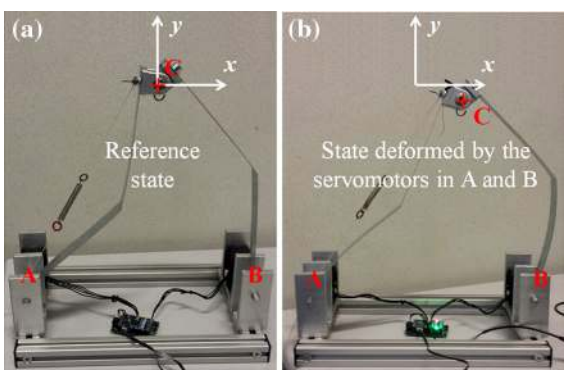

Fig. 6 Example of configurations of the demonstrator: **a** in the reference configuration, **b** for a configuration $\theta_A = 12°$ and $\theta_B = -27°$, resulting from the actuation of the two servomotors

Construction of compliance maps at ambient temperature, i.e. in martensitic (non-activated) state

6. Still at ambient temperature, two angle setpoints are given for the two servomotors situated at joints A and B. Effector C of the structure moves, due to the flexibility of the beams. For example, Fig. 6b shows the configuration for $\theta_A = 12°$ and $\theta_B = -27°$ (outside of the range for better visibility).
7. The coordinates (x, y) of the point attained by the effector are measured using the laser tracker.
8. A vertical load $F_y = -3$ N is applied using a mass suspended from the effector. The effector moves to a new position.
9. The new coordinates (x', y') are measured using the laser tracker.
10. The difference between (x', y') and (x, y) makes it possible to deduce the displacement of the effector. It is thus possible to calculate the two global compliances at point (x, y) of the pseudo-workspace:

$$S_{xy}^{non-act} = (x' - x)/F_y \quad (1)$$

$$S_{yy}^{non-act} = (y' - y)/F_y \quad (2)$$

11. Steps 6–10 are repeated with a new setpoint on θ_A and θ_B. A survey of the eleven values for each angle enables the map of $S_{xy}^{non-act}$ and $S_{yy}^{non-act}$ to be obtained by interpolation.

Construction of compliance maps at high temperature, i.e. in austenitic (activated) state

12. The SMA spring is heated by passing an electric current through it.
13. The same steps are repeated from 6 to 11 while maintaining Joule heating in the SMA spring.

3 Results and analysis

This section presents the results obtained using the experimental procedure described above. Section 3.1 shows the pseudo-workspaces obtained in the non-activated and activated states of the SMA component, for both cases #1 and #2. Sections 3.2 and 3.3 are

dedicated to the analysis of the compliance maps, for case #1 and case #2 respectively.

3.1 Analysis of the pseudo-workspaces

Before presenting the compliance maps, let us describe the pseudo-workspaces of the mechanism in each state (non-activated and activated, i.e. in martensitic and austenitic states respectively), for both cases #1 and #2. These spaces are obtained with the laser tracker by using 11×11 values for θ_A and θ_B in the interval $[-12°, +12°]$, see Sect. 2.3. Figure 7 shows the 11×11 points reached by point C, enabling us to visualize the pseudo-workspaces obtained for case #1 (SMA component pre-stretched by 6%, see Table 5). The following comments can be made:

- Figure 7a shows the pseudo-workspace for the non-activated configuration ($\mathrm{PWS}_{6\%}^{\mathrm{non-act}}$). The 11×11 points appear to be quite regularly spaced,
- Figure 7b shows the pseudo-workspace in the activated configuration ($\mathrm{PWS}_{6\%}^{\mathrm{act}}$). The dimensions of $\mathrm{PWS}_{6\%}^{\mathrm{act}}$ are much smaller those of $\mathrm{PWS}_{6\%}^{\mathrm{non-act}}$,
- Figure 7c shows the consistency of the common space $\mathrm{PWS}_{6\%}$ between the two pseudo-workspaces: $\mathrm{PWS}_{6\%} = \mathrm{PWS}_{6\%}^{\mathrm{non-act}} \cap \mathrm{PWS}_{6\%}^{\mathrm{act}} \neq \varnothing$. The points of this space can therefore be reached in both configurations (non-activated and activated).

The same analysis can be made for case #2, i.e. without the pre-stretch of the SMA component: see Fig. 8. Here too, a common space $\mathrm{PWS}_{0\%}$ is obtained between the non-activated and activated configurations: $\mathrm{PWS}_{0\%} = \mathrm{PWS}_{0\%}^{\mathrm{non-act}} \cap \mathrm{PWS}_{0\%}^{\mathrm{act}} \neq \varnothing$ (see Fig. 8c).

It can be noted that both pseudo-workspaces $\mathrm{PWS}_{6\%}^{\mathrm{act}}$ and $\mathrm{PWS}_{0\%}^{\mathrm{act}}$ are smaller than in the non-activated configuration. This is due to the increase in the Young's modulus of the material during the

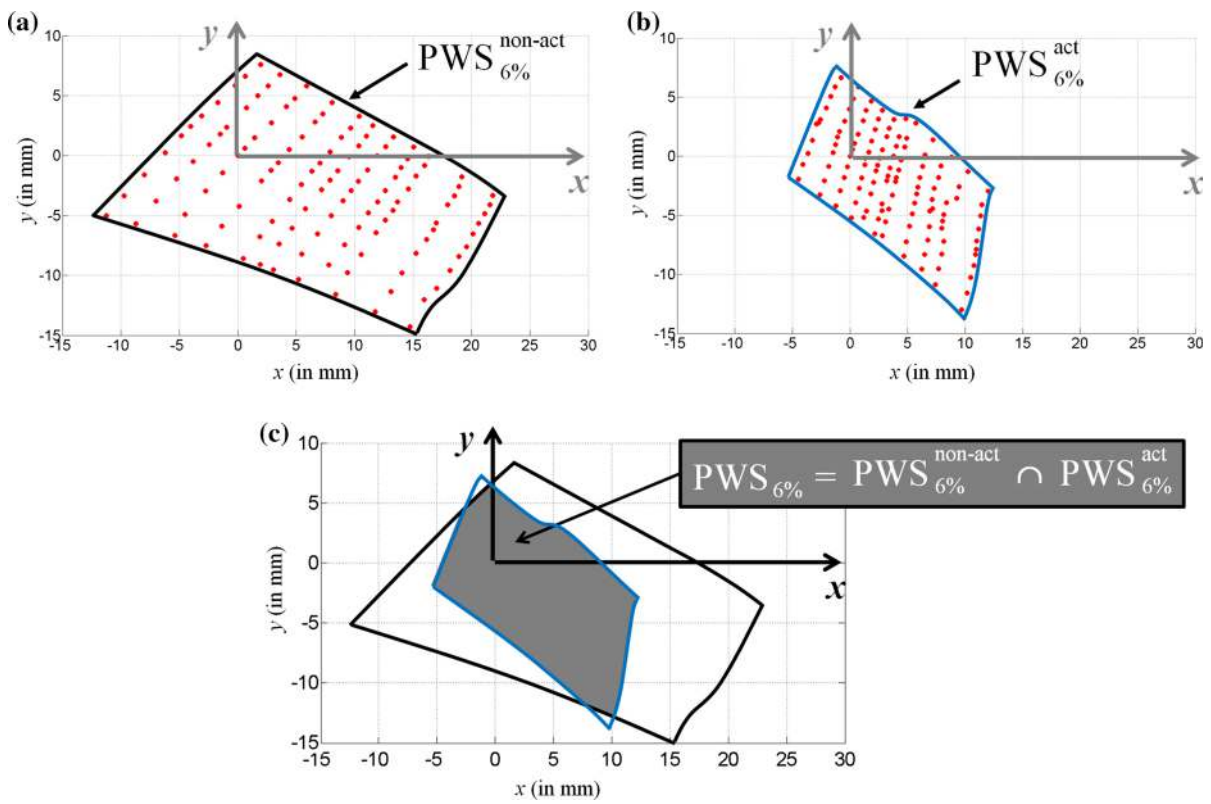

Fig. 7 Pseudo-workspaces in case #1: **a** with SMA in the martensitic state, i.e. in the non-activated state, **b** with SMA in the austenitic state, i.e. in the activated state, **c** intersection between the two pseudo-workspaces

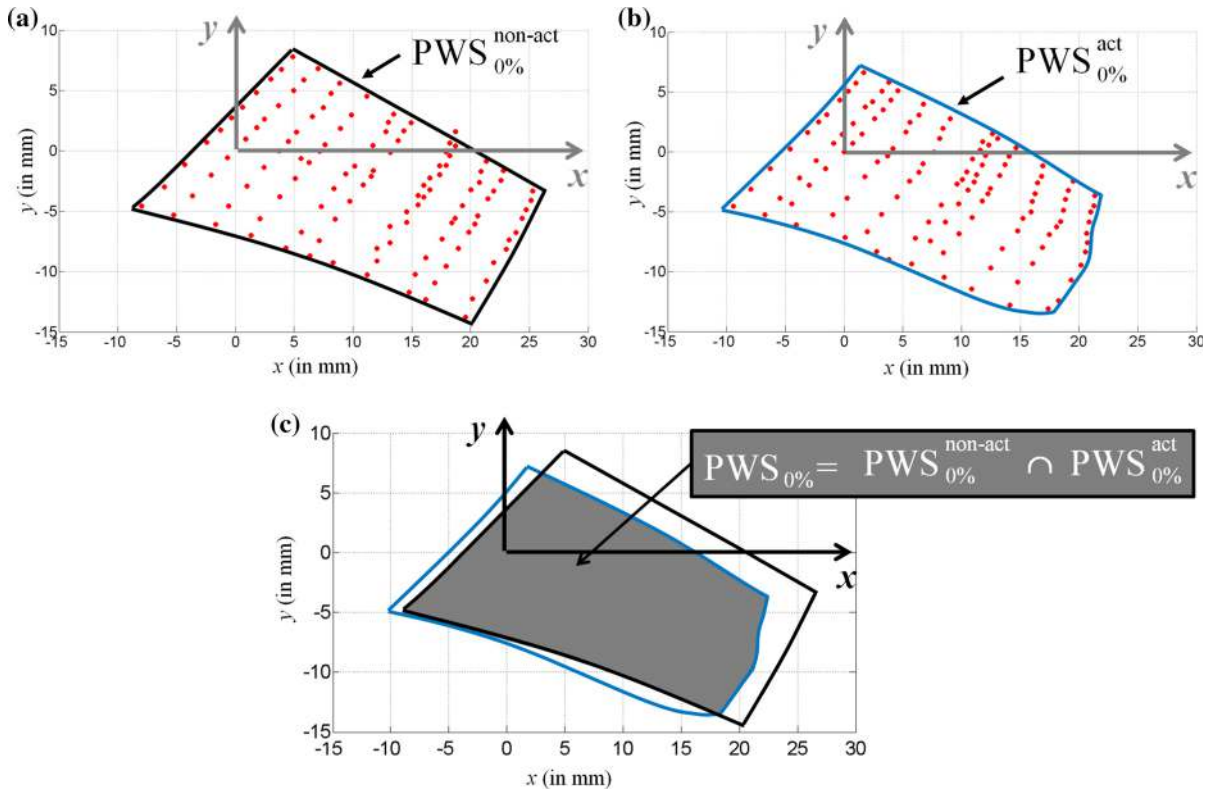

Fig. 8 Pseudo-workspaces in case # 2: **a** with SMA in the martensitic state, i.e. in the non-activated state, **b** with SMA in the austenitic state, i.e. in the activated state, **c** intersection between the two pseudo-workspaces

transformation from martensite to austenite: $K_{act} > K_{non-act}$ (see Table 3). As a consequence, the mechanism is less flexible when the SMA component is in the austenitic state than in the martensitic state.

3.2 Compliance maps in case #1

We now present the results of the tests performed on the device when the SMA spring was pre-stretched by 6%. Compliance maps were obtained by interpolation from a finite number of points in the activated and non-activated workspaces. Therefore, some differences may appear between the continuous and discrete representations of the common workspace (depending on the zone extrapolated around the points). Figure 9 shows the results for the *yy* compliance component. The following comments can be made:

- Figure 9a, b presents the $S_{yy}^{non-act}$ and S_{yy}^{act} compliance maps respectively, each plotted in its respective pseudo-workspace ($PWS_{6\%}^{non-act}$ and $PWS_{6\%}^{act}$). The extreme values are close:$\max(S_{yy}^{non-act}) = 2.45$ mm/N, $\max(S_{yy}^{act}) = 2.20$ mm/N and $\min(S_{yy}^{non-act}) = \min(S_{yy}^{act}) = 1$ mm/N. However, these maximum and minimum values are not obtained at the same locations in the space,
- Figure 9c show the mapping of the compliance ratio R_{yy} (with $R_{yy} = S_{yy}^{act}/S_{yy}^{non-act}$). It is noted that this ratio is positive over the whole $PWS_{6\%}$. It is also observed that the ratio varies from 0.82 to 1.40, which is to say that the passage of the SMA component from martensitic to austenitic changes the compliance between -18% and +40% depending on the location under consideration in the space. This result validates experimentally the concept of varying compliance, at the same point in the pseudo-workspace, of a mechanism integrating an SMA component.

Figure 10 provides the maps for the *xy* compliance component, still for case #1. Figure 10a, b shows the compliance maps for $S_{xy}^{non-act}$ and S_{xy}^{act} respectively. For

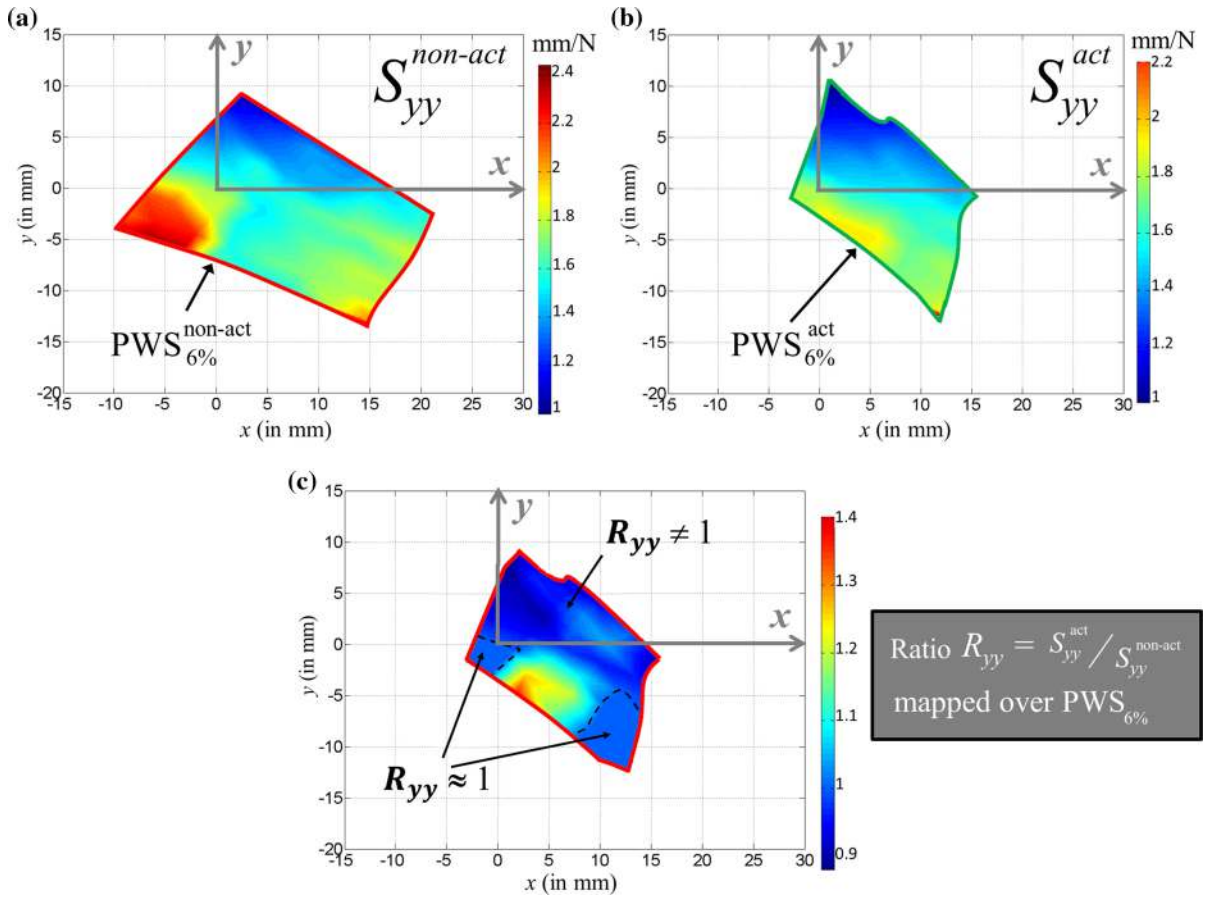

Fig. 9 Compliance map S_{yy} for case #1: **a** with SMA in the martensitic state, i.e. in the non-activated state, **b** with SMA in the austenitic state, i.e. in the activated state, **c** compliance ratio R_{yy} on PWS$_{6\%}$

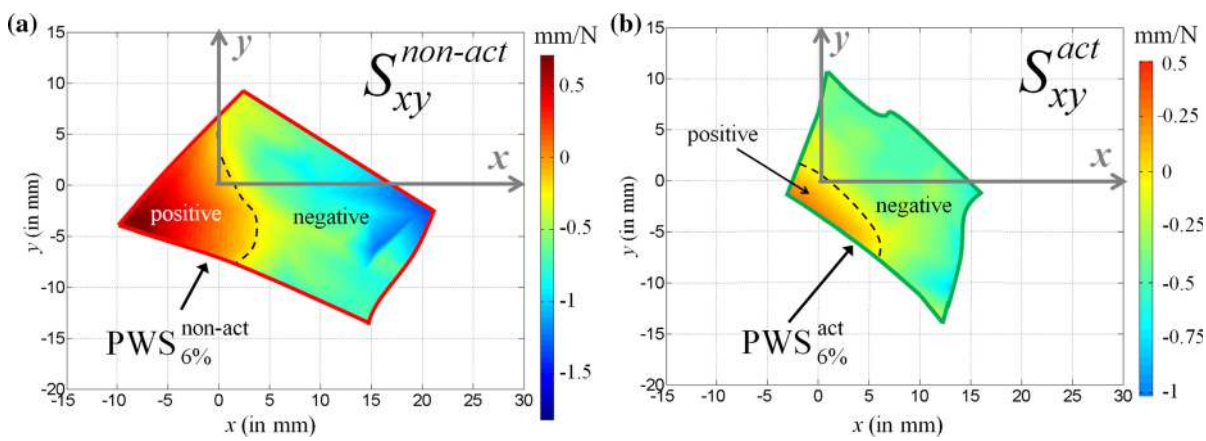

Fig. 10 Compliance maps S_{xy} for case #1: **a** with SMA in the martensitic state, i.e. in the non-activated state, **b** with SMA in the austenitic state, i.e. in the activated state

both maps, there is a gradient from negative to positive values. The maximum values are quite close on both maps: $\max(S_{xy}^{non-act}) = 0.65$ mm/N and $\max(S_{xy}^{act}) = 0.50$ mm/N. On the other hand, there is a clear difference for the minimum values: $\min(S_{xy}^{non-act}) = -1.80$ mm/N and $\min(S_{xy}^{act}) = -1$ mm/N. We see that $S_{xy}^{non-act}$ and S_{xy}^{act} can be of negative or positive sign. This prevents the clear representation of the ratio R_{xy}, with $R_{xy} = S_{xy}^{act}/S_{xy}^{non-act}$, since it takes infinite values for $S_{xy}^{non-act} = 0$. To better analyze the variation in this compliance, three maps are provided in Fig. 11:

- the distribution of the sign of R_{xy} is first presented in Fig. 11a. The values are positive, except in a thin sliver splitting the pseudo-workspace into two and where $R_{xy} < 0$. Lines where $R_{xy} = \pm\infty$ and $R_{xy} = 0$ are also present,
- Figure 11b shows the areas where R_{xy} is different from 1. It can be seen in this figure that the compliance varies over the majority of the space, which is a good feature,
- Figure 11c shows the difference $S_{xy}^{act} - S_{xy}^{non-act}$. This difference varies between -0.31 mm/N and 0.4 mm/N, which evinces a large variation between the two states of the SMA component compared to the absolute values.

3.3 Compliance maps in case #2

The same analysis was performed for case #2, i.e. with no pre-stretch of the SMA (self-accommodating martensitic state). Figure 12 shows the results for the *yy* compliance component:

- Figure 12a, b presents the compliance maps $S_{yy}^{non-act}$ and S_{yy}^{act} respectively. Overall, the compliance values were higher in case #1 than in case #2 (compare with Fig. 9a, b): the mechanism was on the whole more flexible when the SMA spring was pre-stretched. Note also that the compliances vary essentially as a function of the vertical coordinate *y*,
- Figure 12c shows the map of the ratio $R_{yy} = S_{yy}^{act}/S_{yy}^{non-act}$. The latter varies between 0.87 and 1.35, which is to say that R_{yy} varies between -13% and 35% depending on the point in space. When comparing with case #1 (see Fig. 9), a reduction in the compliance ratio is observed: pre-stretching the SMA component increased the variability over time of the overall compliance of the mechanism.

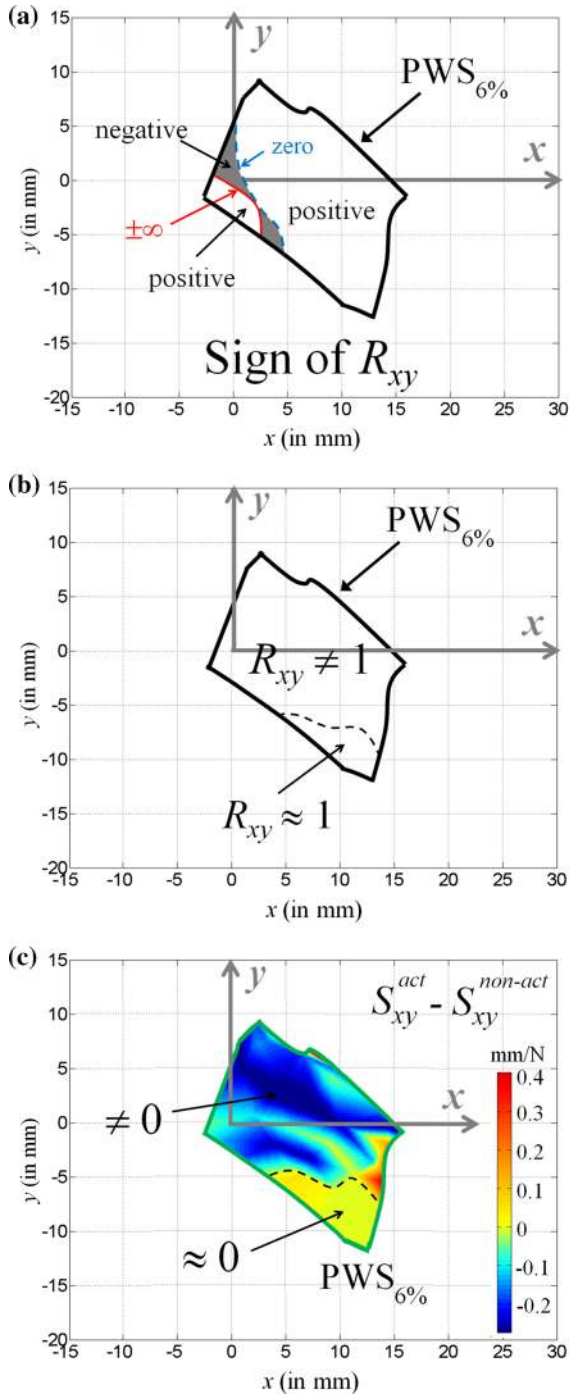

Fig. 11 Analysis of the change in *xy* compliance for case #1: **a** sign of the compliance ratio R_{xy}, **b** zones for which R_{xy} is different from 1, **c** map of the difference $S_{xy}^{act} - S_{xy}^{non-act}$

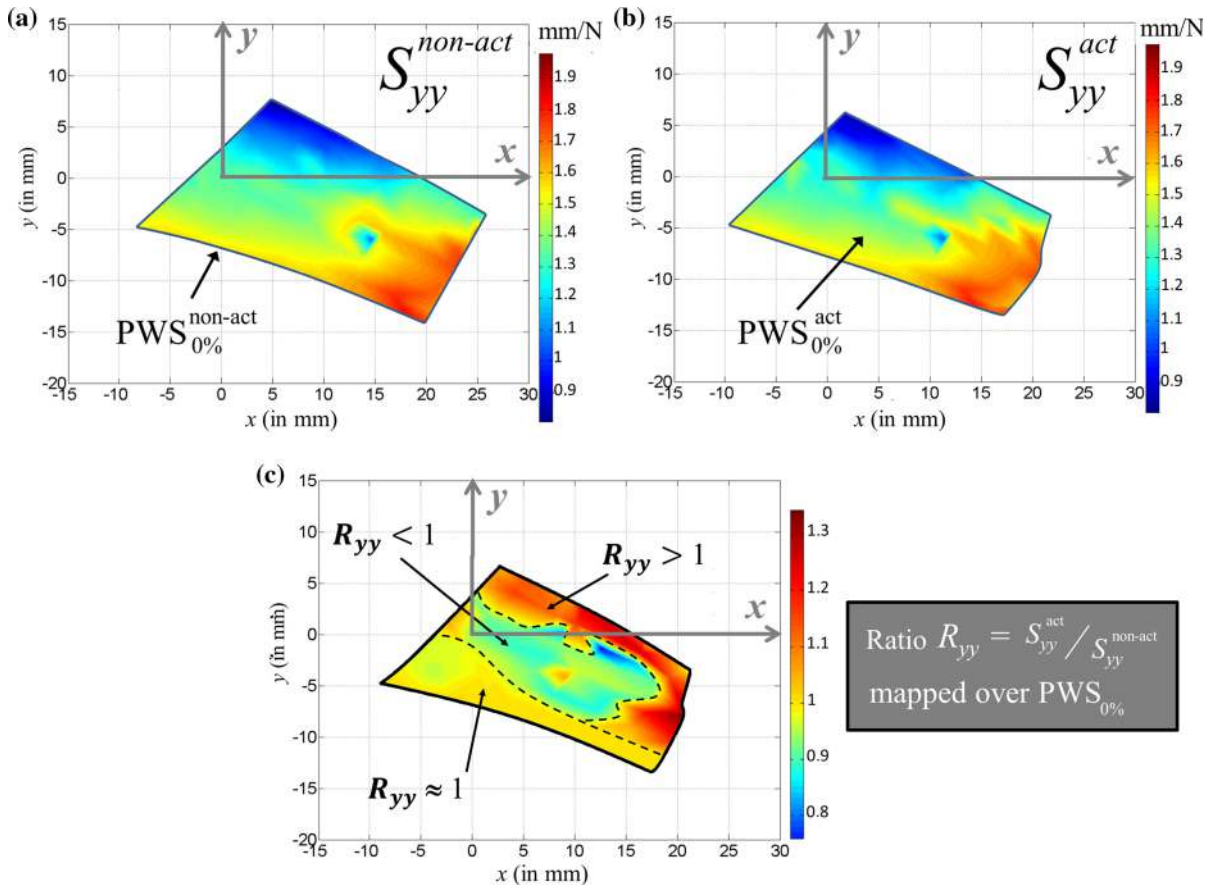

Fig. 12 Compliance maps S_{yy} for case #2: **a** with SMA in the martensitic state, i.e. in the non-activated state, **b** with SMA in the austenitic state, i.e. in the activated state, **c** compliance ratio R_{yy} on $PWS_{0\%}$

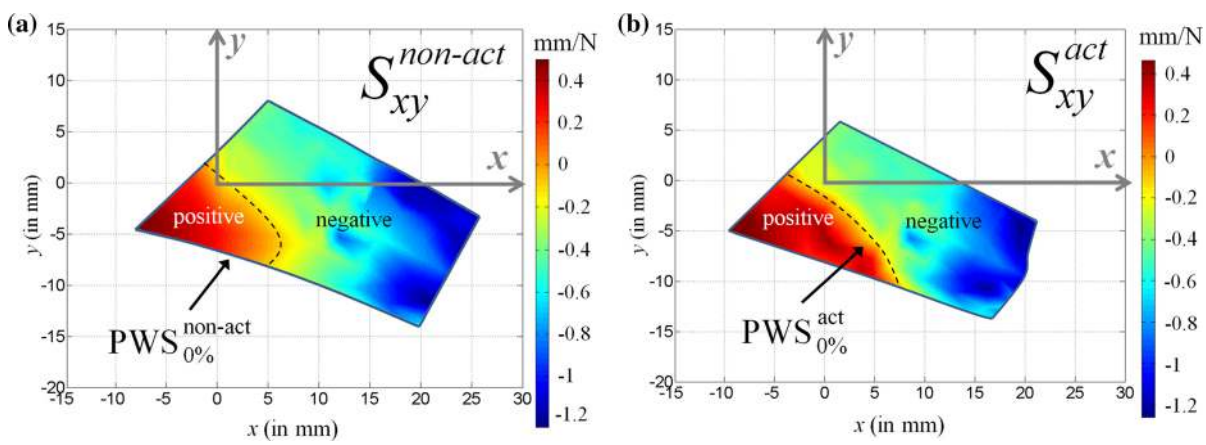

Fig. 13 Compliance maps S_{xy} for case #2: **a** with SMA in the martensitic state, i.e. in the non-activated state, **b** with SMA in the austenitic state, i.e. in the activated state

Finally, as for case #1, there is an area in the pseudo-workspace where the ratio does not vary ($R_{yy} \simeq 1$).

Figure 13 provides the results for the other compliance component (xy). Figure 13a, b shows the compliance maps for $S_{xy}^{non-act}$ and S_{xy}^{act}, respectively. The compliance distribution varies mainly as a function of the horizontal coordinate x, in contrast to the maps of component yy, where compliance varied essentially as a function of y, evincing anisotropy in the stiffness distribution variation.

Figure 14 provides an analysis of the compliance ratio R_{xy}:

- Figure 14a shows the distribution of the sign of R_{xy}. The presence of a negative zone shows the possibility of changing the sign of the compliance at the same point in the pseudo-workspace by transferring the SMA component from one configuration to another,
- in Fig. 14b, the compliance variation zone (area where $R_{xy} \neq 1$) occupies a large part of the pseudo-workspace, which is a good feature. Proportionally, however, the zone where $R_{xy} \neq 1$ is smaller when the SMA component is not pre-stretched,
- Figure 14c shows the map of the difference $S_{xy}^{act} - S_{xy}^{non-act}$. A variation ranging from -0.21 mm/N to 0.32 mm/N is observed. In comparison with case #1 (compare with Fig. 11c), this variation is less significant. This confirms the impact of the pre-stretch of the SMA spring, compared to the impact of the change in Young's modulus, in increasing the compliance variability of the mechanism.

3.4 Comparison with numerical simulations

In this section, we present a comparison between numerical and experimental results. For this, a numerical model that takes into account the dimensional parameters and materials of the physical demonstrator was implemented. The calculation was performed using the tool developed in [53]. Numerical compliance values were calculated at regularly distributed points covering the pseudo-workspaces with and without pre-stretch, in activated and non-activated

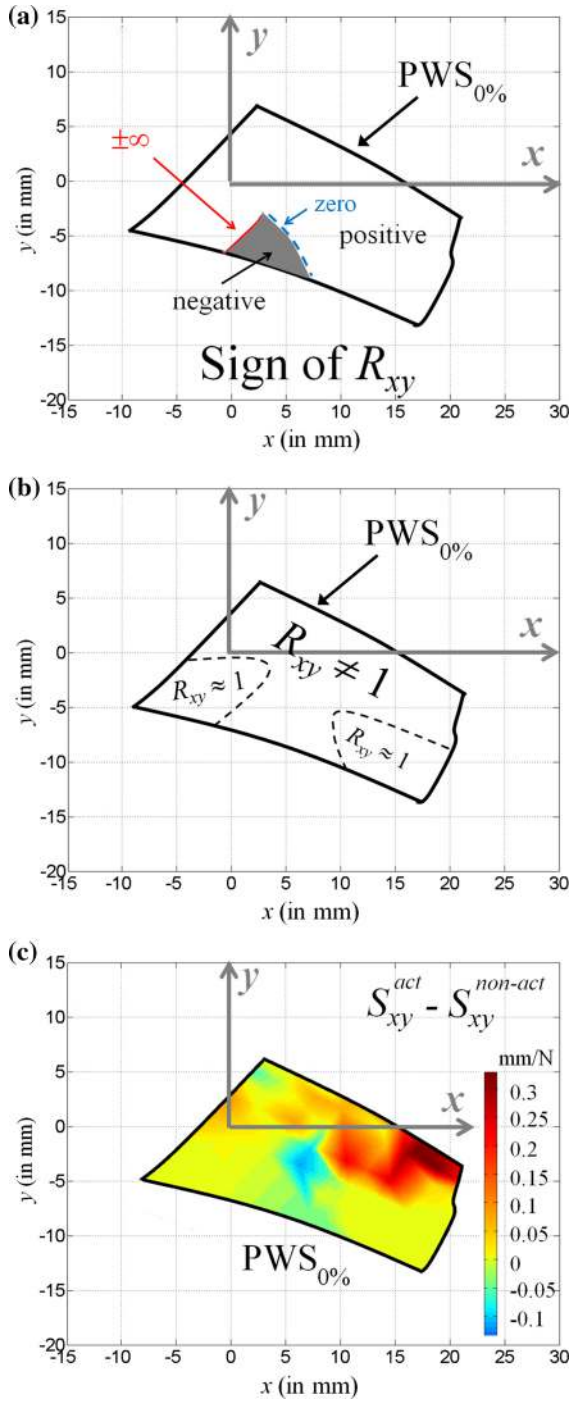

Fig. 14 Analysis of the change in xy compliance for case #2: **a** sign of the compliance ratio R_{xy}, **b** zones for which R_{xy} is different from 1, **c** map of the difference $S_{xy}^{act} - S_{xy}^{non-act}$

configurations. The calculations were made by using the same process as in the experimental procedure.

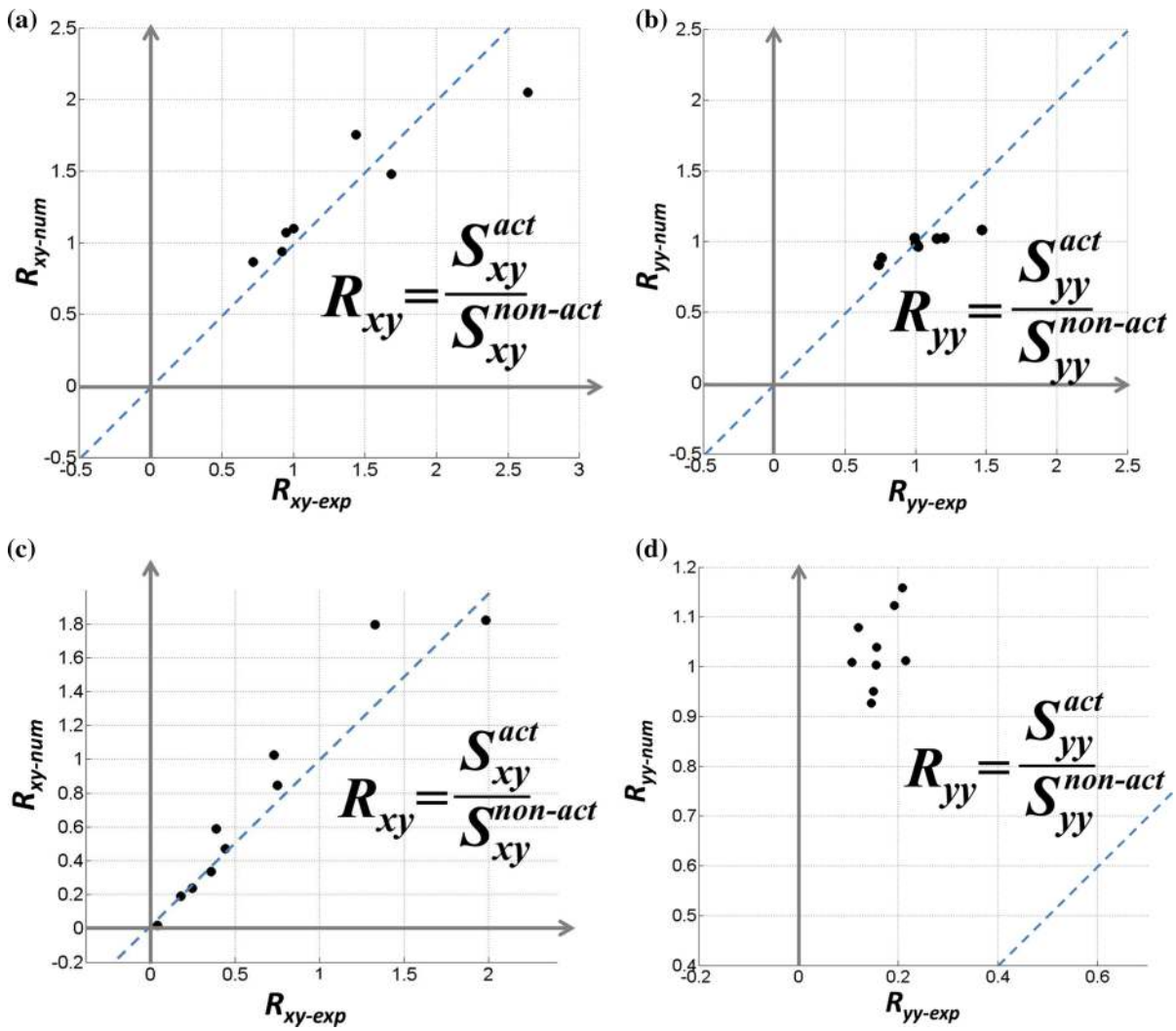

Fig. 15 Numerical-experimental comparison with a pre-strech of: **a**, **b** 0% and **c**, **d** 6%

Figure 15a, b presents the comparison with 0% pre-stretch of the SMA component:

- Fig. 15a present the numerical compliance ratio values R_{xy-num} as a function of those of the experimental compliance ratio R_{xy-exp}. It can be observed that the points follow the bisector, indicating that the numerical and experimental results are in very good agreement,
- the same remarks can be made for the other component (yy): see Fig. 15b: the numerical model enables the compliance variation of the demonstrator to be estimated.

Figure 15c, d presents the numerical-experimental comparison with a 6% pre-stretched SMA component: the points are well aligned along lines. However, for Fig. 15d, deviations from the bisector are larger than for the case without pre-stretch. We consider that this phenomenon originates in the position control of the motors. Indeed, we did not know for a given configuration of the mechanism how the set of forces is established in joints A and B with respect to those related to the deformation of the structure and the stress in the SMA when shape memory is activated. The force equilibrium is thus possibly different from that of the model.

The observed differences could be reduced by adjusting some of the numerical parameters. Improvements by further modeling of the SMA behavior and control would bring numerical predictions closer to experimental values. However, the model correctly reproduced the overall response of the demonstrator in terms of pseudo-workspace consistency and stiffness variability.

4 Conclusion

This paper described the design and the experimental evaluation of a compliant mechanism consisting of a structure based on two flexible angled beams, two rotary actuators, and a shape-memory alloy component. A pseudo-workspace was obtained through the deformation of the structure. The SMA component was thermally actuated in order to change the stiffness at the same points in the pseudo-workspace. Several maps of the compliance along different axes were generated, supporting the principle of the integration of shape-memory alloys in compliant mechanisms to obtain variable stiffness. The main points demonstrated are:

- the possibility of obtaining a common area between the two pseudo-workspaces corresponding to the activated and non-activated modes of the SMA component,
- the existence of interesting properties, such as the anisotropy of the variation in stiffness, or its sign inversion,
- the impact of SMA pre-stretch in the martensitic state on compliance variability.

The experimental results presented here are incentive to build a new framework for the optimization of compliant mechanisms, as well as for the future adjustment of their stiffness with the perspective of performing versatile tasks. The development of map analysis tools inspired by image processing algorithms is the next step towards mechanism design processes which will target controllable properties according to a desired task (for instance variable stiffness over a stroke for an actuator or over a workspace for a manipulator).

The control of the position, orientation and stiffness of the effector, either by closed-form equations, real-time finite element simulations with optimization or learning algorithms, will be an interesting research subject for development in the near future, leading to a significant contribution in the specific field of the control of compliant mechanisms.

Compliance with ethical standards

Conflict of interest The authors declare that they have no conflict of interest.

References

1. Lobontiu N (2002) Compliant mechanisms: design of flexure hinges. CRC Press, Boca Raton
2. Howell LL, Magleby SP, Olsen BM (2013) Handbook of compliant mechanisms. Wiley, Chichester
3. Gong J, Pang J, Zhang Y (2014) Stiffness analysis of a compliant mechanism considering complex deformations of all flexible structure units. Micro Nanosyst 6(3):156–162
4. Ding B, Li Y, Tang Y (2015) Workspace analysis for a 3-DOF compliant parallel mechanism based on SimMechanics. In: 7th International Conference on Cybernetics and Intelligent Systems (CIS) and Conference on Robotics, Automation and Mechatronics (RAM), IEEE, pp 48–53
5. Hao G, Li H (2016) Extended static modeling and analysis of compliant compound parallelogram mechanisms considering the initial internal axial force. J Mech Robot 8(4):041008–041011
6. Yu J, Lu D, Hao G (2016) Design and analysis of a compliant parallel pan-tilt platform. Meccanica 51(7): 1559–1570
7. Zhu WL, Zhu Z, Shi Y, Wang X, Guan K, Ju BF (2016) Design, modeling, analysis and testing of a novel piezo-actuated XY compliant mechanism for large workspace nano-positioning. Smart Mater Struct 25(11):115033
8. Turkkan OA, Su HJ (2017) A general and efficient multiple segment method for kinetostatic analysis of planar compliant mechanisms. Mech Mach Theory 112:205–217
9. Kaminakis NT, Stavroulakis GE (2012) Topology optimization for compliant mechanisms, using evolutionary-hybrid algorithms and application to the design of auxetic materials. Compos Part B Eng 43(6):2655–2668
10. Ivanov I, Corves B (2014) Stiffness-oriented design of a flexure hinge-based parallel manipulator. Mech Based Des Struct Mach 42(3):326–342
11. Hawks JC, Colton MB, Howell LL (2015) A variable-stiffness straight-line compliant mechanism. In: International Design Engineering Technical Conferences (IDETC) and Computers and Information in Engineering Conference (CIE), ASME, V05AT08A011
12. Ayoubi Y, Laribi MA, Courrèges F, Zeghloul S, Arsicault M (2016) A complete methodology to design a safety mechanism for prismatic joint implementation. In: International Conference on Intelligent Robots and Systems (IROS), RSJ/IEEE, pp 304–309

13. Berselli G, Meng Q, Vertechy R, Parenti Castelli V (2016) An improved design method for the dimensional synthesis of flexure-based compliant mechanisms: optimization procedure and experimental validation. Meccanica 51(5):1209–1225
14. Chen G, Chang H, Li G (2016) Design of constant-force compliant Sarrus mechanism considering stiffness nonlinearity of compliant joints. In: Advances in Reconfigurable Mechanisms and Robots II. Springer, Cham, pp 107–116
15. Hongzhe Z, Dong H, Lei Z, Shusheng B (2017) Design of a stiffness-adjustable compliant linear-motion mechanism. Precis Eng 48:305–314
16. Marković K, Zelenika S (2017) Optimized cross-spring pivot configurations with minimized parasitic shifts and stiffness variations investigated via nonlinear FEA. Mech Based Des Struct Mach 45(3):1–15
17. Hao G (2016) Mobility and structure re-configurability of compliant mechanisms. In: Advances in Reconfigurable Mechanisms and Robots II. Springer, Cham, pp 49–60
18. Vanderborght B, Albu-Schäffer A, Bicchi A, Burdet E, Caldwell DG, Carloni R, Catalano M, Eiberger O, Friedl W, Ganesh G et al (2013) Variable impedance actuators: a review. Robot Auton Syst 61(12):1601–1614
19. Manti M, Cacucciolo V, Cianchetti M (2016) Stiffening in soft robotics: a review of the state of the art. IEEE Robot Autom Mag 23(3):93–106
20. Otsuka K, Wayman CM (1999) Shape memory materials. Cambridge University Press, Cambridge
21. Lagoudas DC (2010) Shape memory alloys: modeling and engineering applications. Springer, New-York
22. Lexcellent C (2013) Shape-memory alloys handbook. Wiley, Hoboken
23. Doroudchi A, Zakerzadeh MR, Baghani M (2018) Developing a fast response SMA-actuated rotary actuator: modeling and experimental validation. Meccanica 53(1–2):305–317
24. Sreekumar M, Nagarajan T, Singaperumal M (2009) Application of trained NiTi SMA actuators in a spatial compliant mechanism: experimental investigations. Mater Des 30(8):3020–3029
25. Zakerzadeh MR, Salehi H, Sayyaadi H (2011) Modeling of a nonlinear Euler-Bernoulli flexible beam actuated by two active shape memory alloy actuators. J Intell Mater Syst Struct 22(11):1249–1268
26. Qiu C, Zhang K, Dai JS (2014) Constraint-based design and analysis of a compliant parallel mechanism using SMA-spring actuators. In: International Design Engineering Technical Conferences (IDETC) and Computers and Information in Engineering Conference (CIE), ASME, V05AT08A035
27. Fortini A, Suman A, Merlin M, Garagnani GL (2015) Morphing blades with embedded SMA strips: an experimental investigation. Mater Des 85:785–795
28. Jovanova J, Frecker M, Hamilton RF, Palmer TA (2016) Target shape optimization of functionally graded shape memory alloy compliant mechanism. In: Conference on Smart Materials, Adaptive Structures and Intelligent Systems (SMASIS), ASME, V002T03A006
29. Mammano GS, Dragoni E (2015) Modelling, simulation and characterization of a linear shape memory actuator with compliant bow-like architecture. J Intell Mater Syst Struct 26(6):718–729
30. Kim M, Shin YJ, Lee JY, Chu WS, Ahn SH (2017) Pulse width modulation as energy-saving strategy of shape memory alloy based smart soft composite actuator. Int J Precis Eng Manuf 18(6):895–901
31. Rodrigue H, Wang W, Han MW, Kim TJ, Ahn SH (2017) An overview of shape memory alloy-coupled actuators and robots. Soft Robot 4(1):3–15
32. Yuan H, Fauroux JC, Chapelle F, Balandraud X (2017) A review of rotary actuators based on shape memory alloys. J Intell Mater Syst Struct 28(14):1863–1885
33. Yuan H, Chapelle F, Fauroux JC, Balandraud X (2018) Concept for a 3D-printed soft rotary actuator driven by a shape-memory alloy. Smart Mater Struct 27(5):055005
34. Szewczyk J, Marchandise E, Flaud P, Royon L, Blanc R (2011) Active catheters for neuroradiology. J Robot Mechatron 23(1):105–115
35. Koh JS, Lee DY, Cho KJ (2012) Design of the shape memory alloy coil spring actuator for the soft deformable wheel robot. In: International Conference on Ubiquitous Robots and Ambient Intelligence (URAI), KROS/IEEE, pp 641–642
36. Hadi A, Qasemi M, Elahinia M, Moghaddam NS (2014) Modeling and experiment of a flexible module actuated by shape memory alloy wire. In: Conference on Smart Materials, Adaptive Structures and Intelligent Systems, ASME, V001T03A035
37. Tonapi MM, Godage IS, Walker ID (2014) Next generation rope-like robot for in-space inspection. In: Aerospace Conference, IEEE, pp 1–13
38. Singh P, Ananthasuresh GK (2013) A compact and compliant external pipe-crawling robot. IEEE Trans Robot 29(1):251–260
39. Bharanidaran R, Ramesh T (2014) Numerical simulation and experimental investigation of a topologically optimized compliant microgripper. Sens Actuators Phys 205:156–163
40. Engeberg ED, Dilibal S, Vatani M, Choi JW, Lavery J (2015) Anthropomorphic finger antagonistically actuated by SMA plates. Bioinspir Biomim 10(5):056002
41. She Y, Li C, Cleary J, Su HJ (2015) Design and fabrication of a soft robotic hand with embedded actuators and sensors. J Mech Robot 7(2):021007–021009
42. Li J, Zu L, Zhong G, He M, Yin H, Tan Y (2017) Stiffness characteristics of soft finger with embedded SMA fibers. Compos Struct 160:758–764
43. Shivaram AC, Thakare AG, Buravalla VR, Suryanarayan S (2012) Stiffness control using smart actuators. U.S. Patent 8,313,108
44. Brailovski V, Facchinello Y, Brummund M, Petit Y, Mac-Thiong JM (2016) Ti–Ni rods with variable stiffness for spine stabilization: manufacture and biomechanical evaluation. Shape Mem Superelast 2(1):3–11
45. Heinonen J, Vessonen I, Klinge P, Järvinen E (2008) Controlling stiffness of a frame spring by changing the boundary condition with an SMA actuator. Comput Struct 86(3):398–406
46. Dieng L, Helbert G, Chirani SA, Lecompte T, Pilvin P (2013) Use of shape memory alloys damper device to mitigate vibration amplitudes of bridge cables. Eng Struct 56:1547–1556
47. Henry CP (2013) Variable stiffness joint mechanism. U.S. Patent 8,475,074

48. Naselli GA, Rimassa L, Zoppi M, Molfino R (2017) A variable stiffness joint with superelastic material. Meccanica 52(4–5):781–793
49. Gao X, Burton D, Turner TL, Brinson LC (2006) Finite element analysis of adaptive-stiffening and shape-control SMA hybrid composites. J Eng Mater Technol 128(3): 285–293
50. Chenal TP, Case JC, Paik J, Kramer RK (2014) Variable stiffness fabrics with embedded shape memory materials for wearable applications. In: International Conference on Intelligent Robots and Systems (IROS), RSJ/IEEE, pp 2827–2831
51. Yuen MC, Bilodeau RA, Kramer RK (2016) Active variable stiffness fibers for multifunctional robotic fabrics. IEEE Robot Autom Lett 1(2):708–715
52. Ransley M, Smitham P, Miodownik M (2017) Active chainmail fabrics for soft robotic applications. Smart Mater Struct 26:08LT02
53. Mekaouche A, Chapelle F, Balandraud X (2016) Using shape memory alloys to obtain variable compliance maps of a flexible structure: concept and modeling. Meccanica 51(6):1287–1299
54. Rizk R, Fauroux JC, Mumteanu M, Gogu G (2006) A comparative stiffness analysis of a reconfigurable parallel machine with three or four degrees of mobility. J Mach Eng 6(2):45–55
55. Bonnemains T, Chanal H, Bouzgarrou BC, Ray P (2009) Stiffness computation and identification of parallel kinematic machine tools. J Manuf Sci Eng 131(4):041013
56. Zhang J, Zhao Y, Dai J (2014) Compliance modeling and analysis of a 3-RPS parallel kinematic machine module. Chin J Mech Eng 27(4):703–713
57. Nguyen AV, Bouzgarrou BC, Charlet K, Béakou A (2015) Static and dynamic characterization of the 6-Dofs parallel robot 3CRS. Mech Mach Theory 93:65–82
58. Mekaouche A, Chapelle F, Balandraud X (2016) Identification of material and joint properties based on the 3D mapping of the Quattro static stiffness. In: Research in interactive design (vol 4): mechanics, design engineering and advanced manufacturing. Springer, pp 579–584
59. Mekaouche A, Chapelle F, Balandraud X (2015) FEM-based generation of stiffness maps. IEEE Trans Robot 31(1):217–222